Phase and amplitude reconstruction in single-pixel transmission microscopy: a comparison between Hadamard, cosine and noiselet basis

A. Santos-Amador[1,**], **M. Araiza-Esquivel**[2,*], **H. González**[2,3], **A. Rodríguez-Cobos**[1], **E. Tajahuerce**[3], **LL. Martínez-León**[3], **G. Ramírez-Flores**[1], **and R. E. Balderas-Navarro**[1,***]

[1] *Instituto de Investigación en Comunicación Óptica (IICO-UASLP), Av. Karakorum 1470, Lomas 4ta. Secc., San Luis Potosí C.P. 78210, Mexico.*
[2] *Unidad Académica de Ingeniería Eléctrica, Benemerita Universidad Autónoma de Zacatecas, Jardín Juárez 147, Zona Centro, Zacatecas, C.P. 98000, Mexico*
[3] *GROC-UJI, Institute of New Imaging Technologies (INIT), Universitat Jaume I, Avda. Sos Baynat s/n, 12071 Castelló, Spain.*
[*] *Corresponding author: araizama@auz.edu.mx*
[**] *a253595@alumnos.uaslp.mx*
[***] *raul.balderas@uaslp.mx*

Hadamard, cosine, and noiselet basis are implemented into a digital holographic microscope based on single-pixel imaging with the capability to retrieve images of complex objects. The object is illuminated with coherent light modulated with different patterns deployed in a digital micromirror device, and the resulting fields are captured by single-pixel detection. For amplitude images, the experimental results of the three basis are evaluated with the peak signal-to-noise ratio criteria. It is shown that the cosine basis recovers amplitude distributions with the best quality. Regarding phase images, the recovered ones compare well with those obtained with a CMOS camera. © 2021 Optical Society of America

OCIS codes: (090.1995) Digital Holography;(110.0180) microscopy;(070.2025) Discrete optical signal processing {Single Pixel};(250.4745) Optical processing devices;(230.6120) Spatial light modulators {DMD};(090.1000) Aberration Compensation.

http://dx.doi.org/10.1364/ao.XX.XXXXXX

1. INTRODUCTION

Digital holography (DH) has opened a door for many applications, such as phase microscopy for biomedical imaging and optical metrology [1–11]. However, the cost of conventional cameras depends on the operating wavelength, increasing costs for non-visible wavelengths. An alternative is to use the single-pixel (SP) scheme, which resorts to a non-spatial resolution image sensor for registration, providing a low-cost imaging technique that can work in a wide spectral band [12–17]. In addition, it has been shown that SP cameras are capable to work in low light environments [5, 18–20]. Jointly with compressive sensing (CS) it is possible to decrease the number of measurements and the imaging recording time [14, 15, 18, 21–23].

Several techniques based on single-pixel imaging (SPI) are being developed for different applications, such as microscopy [12, 19, 21, 24, 25], edge detection [26], imaging through dispersive media [5, 18, 27, 28], computational color imaging [14, 24, 29], computational ghost imaging [30], among others [31, 32]. In particular, the SPI techniques have been applied for phase and complex amplitude imaging using both noninterferometric and interferometric approaches. Regarding noninterferometric techniques, we can mention methods based on

coherent diffraction [33], wavefront sampling with position sensing detectors [6], the transport of intensity equation [34], or reference-free holography [35]. Concerning interferometric approaches, in general all the methods are based on optical interferometers combining an SLM sampling the complex pattern to be reconstructed with single-pixel detection. Among the different optical architectures, we can distinguish ghost imaging [22], Mach-Zehnder interferometers [28], Michelson interferometers with phase encoded reference beams [36, 37], or common path interferometers [37].

The SPI technique consists in projecting a series of microstructured light patterns onto a sample, while a photodetector without spatial resolution records the light intensity associated to each pattern. In general, the object is sampled with functions comprising an orthogonal basis codified on a spatial light modulator (SLM). Based on the measurements and using a computational algorithm, the final image is reconstructed numerically. The approach based on Hadamard single-pixel imaging (HSI) calls for a deterministic model using functions of the Hadamard basis for sample illumination [6, 12, 18, 19, 21, 22, 27, 28, 36, 38, 39]. Recent studies have reported on the cosine and noiselet functions as an alternative for the sampling patterns [25, 29, 40, 41].

Furthermore, due to the sparsity of natural scenes when expressed in the Hadamard and cosine basis functions, they are considered for image compression [12, 25, 29, 38] and are good option for applying CS [21, 22, 42, 43]. In addition, functions of the noiselet basis have played a role due to its incoherence with the Haar basis [44, 45]. Therefore, they are considered in CS algorithms as well [42, 45].

Despite these impressive results on phase imaging with SPI, a study of different sampling strategies in a microscope configuration has not yet been accomplished. The purpose of the present paper aims to tackle such issue by a systematic comparison between a commonly employed basis for image reconstruction, the Hadamard one, with less common basis, such as the cosine and noiselet ones.

In this paper, functions of the Hadamard, cosine, and noiselet basis are used as sampling patterns in a digital holographic microscopy setup based on SPI, aimed to shed light on the capability to retrieve amplitude and phase of complex objects. A digital micromirror device (DMD) is integrated into a Mach Zehnder interferometer and is used to modulate the wavefront and to sample the object under study. The system operates in two ways. In the first mode, without using the reference arm, the light patterns modulated by the DMD are projected directly on the object and the system retrieves only amplitude images. The quality of the experimental results, using the Hadamard, cosine, and noiselet basis functions, is validated by using the peak signal-to-noise ratio (PSNR) criteria. In the second mode, the system records holograms retrieving both the phase and amplitude of the measured object; in this case, the light patterns projected onto the object are generated by binary digital holograms codified in the DMD using the Lee method [46]. Moreover, this method allows applying phase-shifting to the binary digital hologram.

This paper is organized as follows. In Section 2, the imaging principles and methods of our technique are outlined. In Section 3, the experimental setup is described. In section 4, the experimental results, as well as the evaluation and comparison of results, are discussed. Finally, in Section 5, the conclusions are summarized.

2. PRINCIPLES AND METHODS

A. Single-pixel amplitude imaging

SPI allows capturing images using a detector without spatial resolution by registering the light intensity variations I_i when an object $O(x, y)$ is sampled with a set of sampling patterns $m_i(x, y)$, with $i = 1, 2, \ldots, N^2$; being N^2 the number of pixels of the image. The two main components of this approach are the spatial light modulator (SLM) and the SP detector. For the registration of the amplitude distribution, it is convenient to use binary sampling functions in order to codify them directly onto the DMD. The integrated intensity in the SP detector is expressed as [28]

$$I_i \propto \iint |O(x,y)m_i(x,y)|^2 \mathrm{d}x\mathrm{d}y. \qquad (1)$$

The intensity of the two-dimensional object can be expressed as a linear superposition of the sampling patterns, weighted by the intensity measurements

$$|O(x,y)|^2 = \sum_{i=1}^{N^2} I_i m_i(x,y). \qquad (2)$$

The experimental setup operates in two different ways. In the first one, the reference beam in Fig. 1 is blocked, thus habilitating

solely the object arm of the interferometer. The 4f image formation stage allows sampling the object plane with the desired sampling pattern deployed by the DMD. Such a procedure can be extended to holography allowing to simultaneously register the object in phase and amplitude.
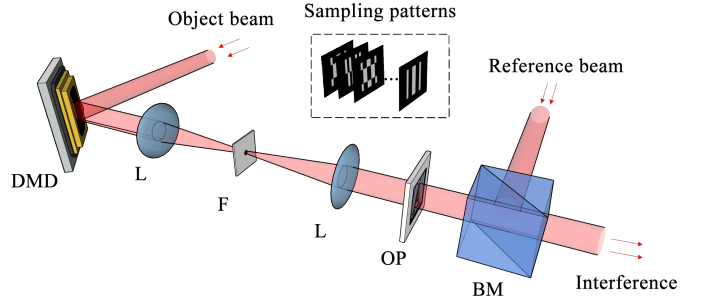
Fig. 1. Single-pixel holographic imaging system. DMD digital micromirror device; L lens; F filter; OP object plane; BM beam splitter. The actual position of the DMD is different than the depicted, as an additional mirror (not shown here) is used to reflect the beam toward the 4f stage.

B. Single-pixel phase imaging

In the second way of operation, the reference arm of the interferometer is enabled causing the constant reference beam R' to interfer with the object amplitude distribution. Now the integrated intensity recorded by the SP detector can be written as

$$y_{i,\varphi} \propto \iint |O(x,y)m_i(x,y)e^{j\varphi} + R'|^2 \mathrm{d}x\mathrm{d}y, \qquad (3)$$

where φ is a constant phase introduced in order to apply the four-step phase-shifting technique. For each pattern i, four intensity values are obtained with $\varphi = 0$, $\varphi = \pi/2$, $\varphi = \pi$, $\varphi = 3\pi/2$. The complex coefficients associated to each complex sample pattern $m_i(x, y)$ are given by [28]

$$Y_i = \frac{1}{4R'}[(y_{i,0} - y_{i,\pi}) + j(y_{i,3\pi/2} - y_{i,\pi/2})], \qquad (4)$$

where $j = \sqrt{-1}$. Finally, the complex object is calculated by the lineal superposition of the sampling patterns, weighted by the complex coefficients in Eq. (4),

$$O(x,y) = \sum_{i=1}^{N^2} Y_i m_i(x,y). \qquad (5)$$

It is important to note that the complex amplitude distribution reconstructed by single-pixel holography is located in the object plane, wherein the sampling patterns are formed. Therefore, in our optical setup, the complex distribution of the object is directly reconstructed without considering light propagation methods.

C. Lee holograms for phase imaging

In order to project a complex sampling pattern $m_i(x, y)$ onto the object, a binary digital hologram codification in the DMD is used. The intensity distribution that results from the interference between the complex pattern with the constant phase of phase-shifting to be projected $m_i(x, y) = A exp[j(\alpha_i(x, y) + \varphi)]$ and a reference plane wave $R exp[j\beta(x + y)]$, is given by [46]

$$t(x,y) = R^2 + A^2 + 2RA \cos[\beta(x+y) + \alpha_i(x,y) + \varphi], \qquad (6)$$

where R and A are the reference wave and object wave amplitude, respectively, β is the carrier frequency and $\alpha_i(x,y)$ is the phase of the pattern. From Eq. (6), being R and A equal to unity, the resultant intensity distribution is given by

$$t(x,y) \propto 1 + \cos[\beta(x+y) + \alpha_i(x,y) + \varphi]. \qquad (7)$$

Eq. (7) allows to apply the well known Lee method to generate off-axis holograms by computer [46]. Binary amplitude holograms $h(x,y)$ are implemented in a DMD by binarizing the function $t(x,y)$ according to

$$h(x,y) = \begin{cases} 1 & if \quad t(x,y) > 0.5, \\ \\ 0 & if \quad otherwise. \end{cases} \qquad (8)$$

The sampling patterns are codified by Eq. (7). Afterward, the binary amplitude hologram is projected by the DMD to modulate the wavefront that propagates toward the 4f stage. At the Fourier plane shown in Fig. 1, a low-pass spatial filter blocks all diffraction orders except the +1 order, hence permitting the desired complex field to be recovered in the object plane. After sampling the object plane, the object light beam interferes with the reference beam and is registered by the photodetector. The phase modulation process calls for the four-step phase-shifting technique in the computer-generated holograms (CGH), thus giving the capacity to register and recover the phase sampled by the patterns.

D. Pattern generation

HSI is based on the Hadamard transform. The method relies on acquiring the Hadamard spectrum of an object when it is sampled with functions of the basis. At the exit of the system, the intensity response is measured by the SP detector. The two-dimensional Hadamard transform $H\{\cdot\}$ of an image $f(x,y)$ is defined as [38]

$$F(u,v) = \sum_{x=0}^{N-1} \sum_{y=0}^{N-1} f(x,y)(-1)^{q(x,y,u,v)}, \qquad (9)$$

where (x,y) are the coordinates in the spatial domain, $N = 2^k$ and

$$q(x,y,u,v) = \sum_{i=0}^{k-1} (u_i x_i + v_i y_i), \qquad (10)$$

where (u,v) are the coordinates of the Hadamard domain. u_i, v_i, x_i, and y_i terms are the binary representations of u, v, x, and y, respectively. $F(u,v)$ is an $N \times N$ size matrix of $+1$ and -1 elements, where the rows and columns fulfill the orthogonality conditions. One way to obtain the $P_H(x,y)$ funtions to sample the object in the spatial domain is by applying the inverse Hadamard transform $H^{-1}\{\cdot\}$ to delta function $\delta(u,v)$ in the Hadamard domain

$$P_H(x,y) = H^{-1}\{\delta(u,v)\}, \qquad (11)$$

where

$$\delta(u,v) = \begin{cases} 1 & if \quad u = u_0, \ v = v_0, \\ \\ 0 & if \quad otherwise. \end{cases} \qquad (12)$$

An example of 16 patterns of the Hadamard basis for $N = 4$ is shown in Fig. 2 (a). As the DMD allows only to modulate binary
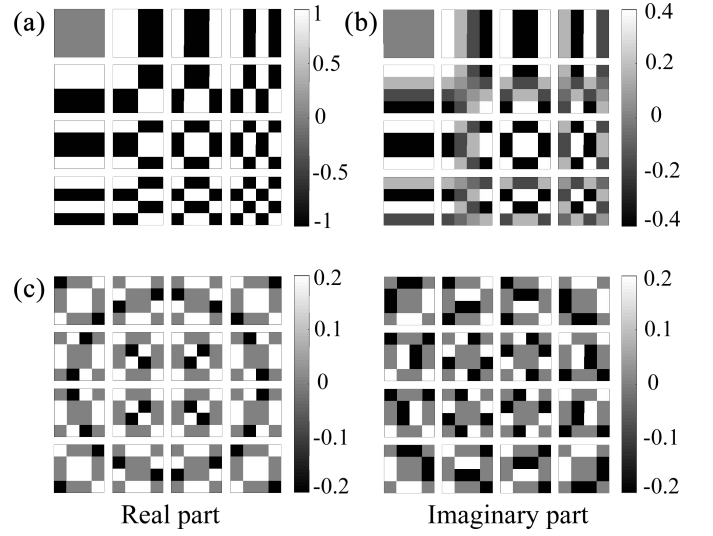
Fig. 2. Basis patterns. (a) Hadamard, (b) cosine and (c) noiselet (real and imaginary parts). See text for details.

elements, the next equation is considered

$$P_H = P_{H^+} - P_{H^-}, \qquad (13)$$

where the P_{H^+} matrix is generated by zeroing every negative element in the P_H matrix, and $P_{H^-} = -(P_H - P_{H^+})$. Such separation in P_{H^+} and P_{H^-} matrices allows direct implementation in the DMD.

The cosine single-pixel image (CSI) system is based on the two-dimensional discrete cosine transform (DCT). The cosine spectrum can be obtained when an object is sampled with patterns of the cosine basis, and its response in intensity is registered with a SP detector. The 2D DCT $C\{\cdot\}$ and the inverse DCT $C^{-1}\{\cdot\}$ of an image $f(x,y)$, of size $N \times N$, are defined as [29]

$$F(u,v) =$$
$$\sum_{x=0}^{N-1} \sum_{y=0}^{N-1} f(x,y)a(u)a(v) \cos\left[\frac{\pi(2x+1)u}{2N}\right] \cos\left[\frac{\pi(2y+1)v}{2N}\right],$$
$$(14)$$

$$f(x,y) =$$
$$\sum_{u=0}^{N-1} \sum_{v=0}^{N-1} F(u,v)a(u)a(v) \cos\left[\frac{\pi(2x+1)u}{2N}\right] \cos\left[\frac{\pi(2y+1)v}{2N}\right],$$
$$(15)$$

with

$$a(u) = \begin{cases} \sqrt{\dfrac{1}{N}}, & u = 0, \\ \\ \sqrt{\dfrac{2}{N}}, & u \neq 0; \end{cases} \qquad a(v) = \begin{cases} \sqrt{\dfrac{1}{N}}, & v = 0, \\ \\ \sqrt{\dfrac{2}{N}}, & v \neq 0, \end{cases} \qquad (16)$$

where $F(u,v)$ is the cosine transform of $f(x,y)$; (x,y) and (u,v) are the coordinates in the spatial and cosine domains, respectively. A pattern of $P_C(x,y)$ can be generated by applying the inverse DCT $C^{-1}\{\cdot\}$ to a delta function $\delta(u,v)$ given by Eq. (12)

$$P_C(x,y) = C^{-1}\{\delta(u,v)\}. \qquad (17)$$

Fig. 2 (b) shows an example of 16 patterns for DCT with $N = 4$. To implement the cosine patterns, it is necessary to apply an

algorithm similar to that used in HSI; namely, $P_C(x,y)$ is divided into P_{C+} and P_{C-} matrices. Therefore, the $P_C(x,y)$ matrix can be expressed as

$$P_C(x,y) = P_{C+} - P_{C-}. \tag{18}$$

By definition of DCT, both P_{C+} and P_{C-} have real values within the range of 0 to +1 and for direct implementation in the DMD, these matrices are binarized by dithering with the Floyd-Steinberg error diffusion algorithm [47]. An example of the dithering method is shown in Fig. 3.
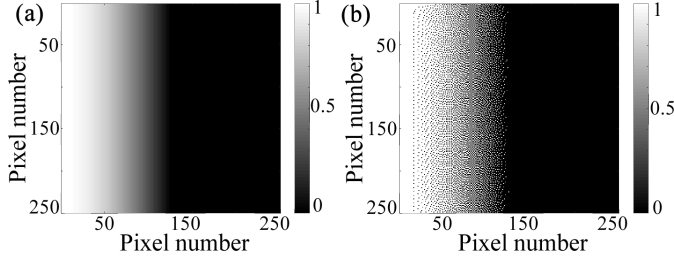
Fig. 3. Positive part of cosine function (a) without dithering and (b) with dithering.

The noiselet matrix is implemented with an iterative process starting with a 1×1 matrix $\mathcal{N}_1 = [1]$; subsequently the noiselet matrices $\mathcal{N}_2, \mathcal{N}_4, \ldots, \mathcal{N}_{2^r}$ of sizes $2 \times 2, 4 \times 4, \ldots, 2^r \times 2^r$, respectively are generated; and r is a positive integer. The iterative procedure for a noiselet matrix of size $N \times N$ is given by

$$\mathcal{N}_N(l,*) = \frac{1}{2}(1-j \; , \; 1+j) \otimes \mathcal{N}_{N/2}\left(\frac{l}{2},*\right), \tag{19}$$

$$l = 0, 2, 4, ..., N-2;$$

$$\mathcal{N}_N(l,*) = \frac{1}{2}(1+j \; , \; 1-j) \otimes \mathcal{N}_{N/2}\left(\frac{l-1}{2},*\right), \tag{20}$$

$$l = 1, 3, 5, ..., N-1,$$

where $(l,*)$ indicates the l-th row vector of $\mathcal{N}_N$, $j = \sqrt{-1}$ and the $\otimes$ symbol is the Kronecker product. Pattern $P_{\mathcal{N}}(x,y)$ can be generated by

$$P_{\mathcal{N}} = mat\left(\mathcal{N}_N(*,t)\right), \tag{21}$$

where $mat(\cdot)$ denotes a square matrix by equally dividing the column vector $(\cdot)$ and stacking it into the corresponding columns of the matrix $P_{\mathcal{N}}$; while $(*,t)$ stands for the t-th column vector of $\mathcal{N}_N$. Fig. 2 (c) shows the real and imaginary parts of 16 patterns of noiselet for $N = 4$.

Unlike HSI and CSI matrices, the noiselet matrix contains complex numbers. Thus, in order to implement the patterns in the DMD, $P_{\mathcal{N}}$ is normalized in such a way that the resulting elements are $+1$, -1, $+j$ and $-j$. Furthermore, they are divided into $P_{\mathcal{N}Re}$ and $P_{\mathcal{N}Im}$ containing the real and imaginary values of $P_{\mathcal{N}}$, respectively. Finally, a similar process to that performed in HSI is used to codify these patterns in the DMD separating from each submatrix the positive and negative parts, thus obtaining four matrices. $P_{\mathcal{N}}$ can be recovered from

$$P_{\mathcal{N}} = (P_{\mathcal{N}Re+} - P_{\mathcal{N}Re-}) + j(P_{\mathcal{N}Im+} - P_{\mathcal{N}Im-}), \tag{22}$$

where the superindex "+" and "−" represent the positive and negative matrices, respectively.

Applying the SPI technique for an image with $N \times N$ pixel resolution, $N \times N \times 2$ patterns are needed in HSI and CSI, whereas for noiselet single-pixel imaging (NSI) $N \times N \times 4$ patterns are required.

E. Comparison among the three basis

The Hadamard and cosine functions basis have been considered in different applications due to the fact that images of natural scenes are sparse in these basis, whereas the noiselet function basis has been shown to be mutual incoherent with respect to the Haar functions, the latter being widely used in CS-based algorithms. Note that the mutual coherence of two basis, $\mu(\Psi, \Phi) = max_{p,q}|\langle\psi_p, \phi_q\rangle|$, is the maximum scalar product of between any pair of basis vectors [44].

The main interest of the methodology used in this work lies in the performance of the SPI system by sampling the object with the three basis described and reconstructing the image by a direct linear superposition. In particular, considering that the cosine function basis needs to be binarized, it would have an associated error in this procedure due to the use of a DMD. However, as shown in the following sections, images obtained with the cosine function basis exhibit the best quality, despite the possible errors associated with such binarization. This reinforces the use of the cosine basis for SP imaging techniques in amplitude mode. In [38] it was shown theoretically and experimentally that Fourier single-pixel imaging (FSI) is more efficient than HSI, while HSI is more robust to noise than FSI. Indeed, in this work it was found that HSI and CSI (*i.e.*, Re(FSI)) offer comparable PSNR results and both are superior to NSI, resulting in good alternatives for SPI systems. Moreover, it is shown that phase images as obtained with SPI compare well to those measured with cameras.

3. EXPERIMENTAL SETUP

Fig. 4 shows the experimental setup based on a Mach-Zehnder interferometer for both operation modes (*i.e.*, SP amplitude imaging and SP phase imaging). The light source is a He-Ne laser (JDSU model 1508-1) with a wavelength of 633 nm filtered and collimated by passing it through a spatial filter and lens. The beam of the laser is divided by a beam splitter, obtaining the object and reference beams. Note that for the amplitude imaging only (first mode), the reference arm is blocked. The object beam falls upon a digital micromirror device (DMD DLP7000) which modulates the wavefront displaying the sampling patterns. The micro-structured modulated wavefront is filtered at the Fourier plane with a lens (focal length = 250 mm) and a spatial filter. Only the +1 order is selected by the transmission aperture of the spatial filter, and a second lens (focal length = 125 mm) together with a 10X microscope objective focuses the sampling patterns in the focal plane the objective. Finally, the object beam with the sample information passes through a second 10X microscope objective up to a second beam splitter. In the second mode the object beam interferes with the reference beam. Finally, in both modes the information generated is focused with a lens and registered with a detector without spatial resolution (Thorlabs APD410A2). The measurement of intensity coefficients is basically a differential measurement process that significantly reduces the influence of noise generated by background lighting to improve the quality of reconstructed images.

The spatial resolution of the SPI system is determined by the pixel size of the sampling light pattern on the sample plane. Consequently, it depends on the size of the pattern codified on the SLM and the magnification of the optical system. In our case, the spatial resolution of the system is 22 μm, that was found experimentally by characterizing the system with a USAF resolution test chart.
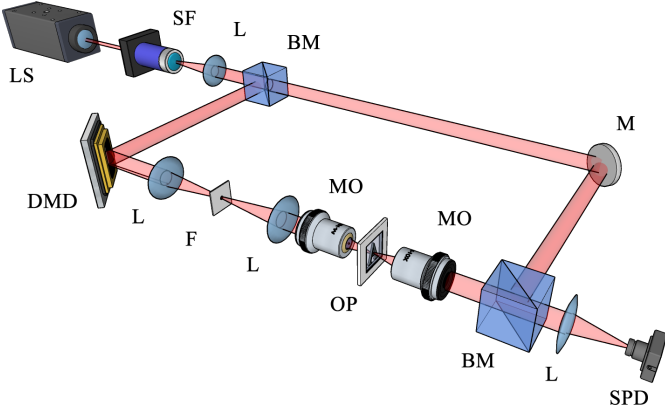
Fig. 4. Experimental setup. LS laser source; SF spatial filter; DMD digital micromirror device; L lens; F filter; OP object plane; BM beam splitter; MO microscope objective; SPD single-pixel detector.

4. EXPERIMENTAL RESULTS

Amplitude and phase of objects were measured by transmission with the described digital holography system based on SPI shown in Fig. 4. The sample was placed in the object plane, where the sampling patterns are displayed. The sampling patterns used in the experiments are generated from the Hadamard, cosine, and noiselet basis as outlined in Section 2.D. For an image with 64×64 pixels resolution, the sampling patterns are scaled by a factor of 8 to cover an area of 512×512 micromirrors of the DMD. In the amplitude SPI-based system, 8192 patterns are displayed in the DMD at a frame rate of 2100 Hz; whereas for the phase SPI-based system, 16384 patterns encoded in binary amplitude holograms are displayed at a frame rate of 4200 Hz. In both methods the recording time for the measurement of the coefficients is about four seconds. Fig. 5 shows a detailed flowchart for the procedures to record and reconstruct both SPI amplitude and phase images.

Fig. 6 shows the experimental results for the reconstruction of the amplitude object. Transparency with the UASLP-University logo is used as the test object, as can be seen in Fig. 6 (a). Figs. 6 (b)-(d) show the corresponding reconstructions for the Hadamard, cosine, and noiselet sampling basis, respectively.

A quantitative comparison of the quality of the reconstructed images is carried out with the PSNR criteria. To analyze the obtained results, the PSNR values are computed along with one dimension of the amplitude distribution. Fig. 7 shows the one-dimensional amplitude distribution corresponding to each basis where the red line indicates the zone of interest (Fig. 6 (a)). The PSNR coefficient is defined by

$$PSNR = 10log_{10} \frac{Max^2}{\frac{1}{NM} \sum_{i=0}^{M} \sum_{j=0}^{N} [U_0(i,j) - U(i,j)]^2}, \quad \textbf{(23)}$$

where U_0 is the ideal amplitude in Fig. 6 (a), with $M \times N$ being the pixels dimension (in our case $M = N$); U is the reconstructed image with different basis, and Max $= 2^8 - 1$ is the maximum value of the image pixels. The PSNR values of the one-dimensional amplitude distribution displayed in Fig. 7, correspond to 7.57, 7.84 and 7.5 dB for Hadamard, cosine and noiselet sampling patterns, respectively. The higher PSNR value the better quality in the reconstructed image. We note that concerning 2D PSNR value, we have calculated them and obtained
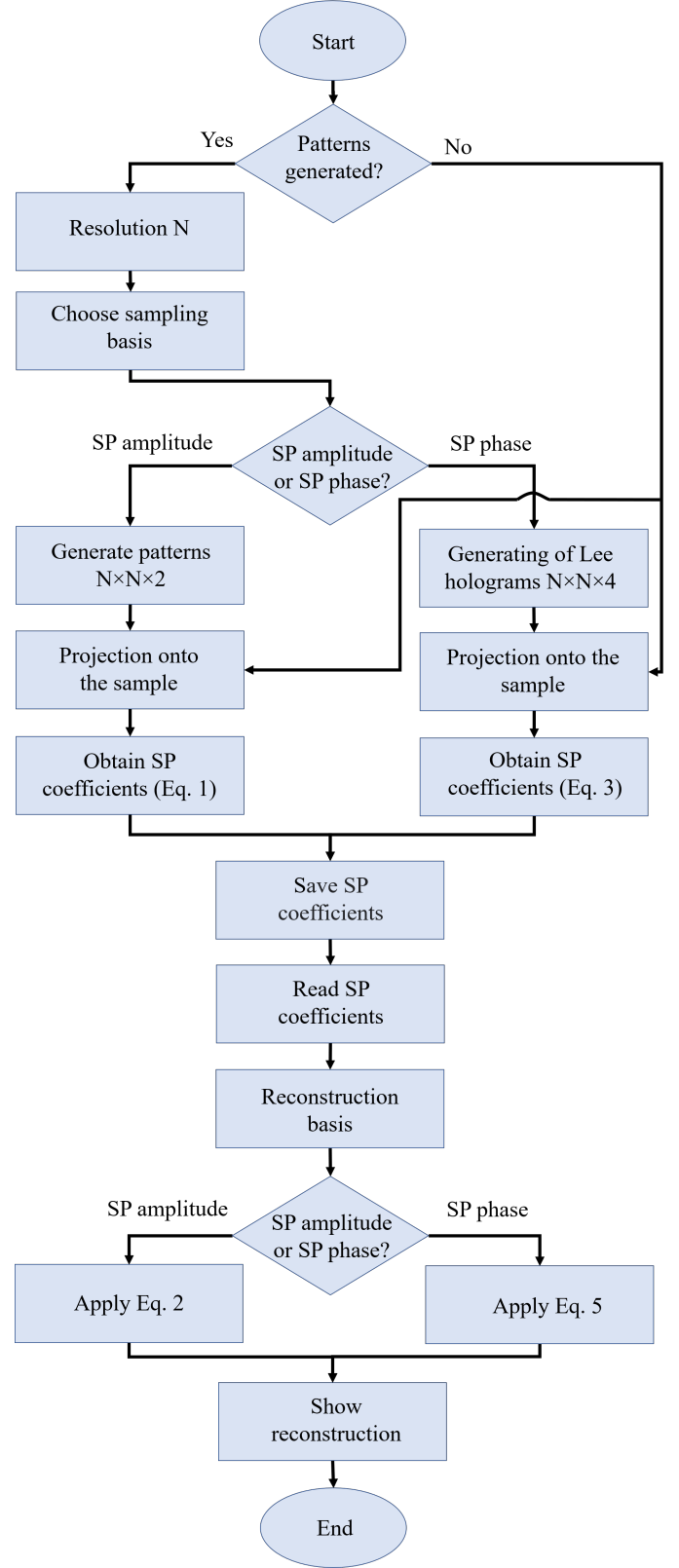

Fig. 5. Flowchart showing the procedure for both amplitude and phase retrieval. See text for details.
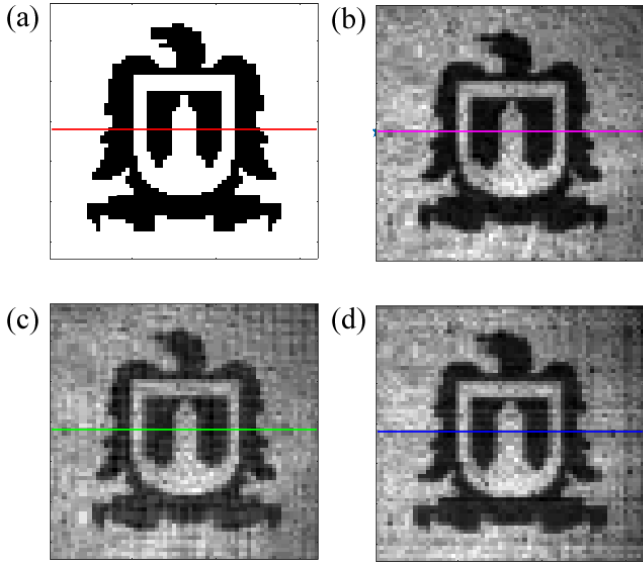
Fig. 6. Amplitude object reconstruction. (a) Transparency with UASLP-University logo. Reconstruction with sampling basis (b) Hadamard, (c) cosine and (d) noiselet.

the following results: 7.61, 7.48, 7.45 dB, for Hadamard, cosine and noiselet cases, respectively. We note that the trend is similar as for the 1D case.

A common characteristic among HSI and CSI is that both coeffi-
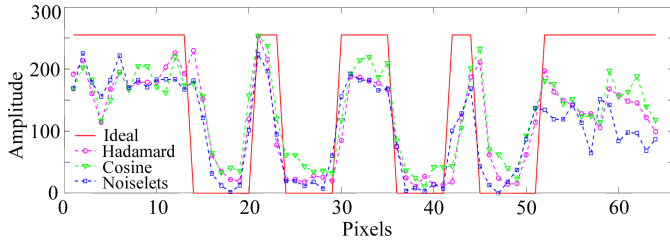
Fig. 7. Experimental results of single-pixel amplitude imaging. One dimensional amplitude distribution along the corresponding lines in Fig. 6. The ideal distribution is shown as a comparison (red line).

cients spectra are sparse signals; *i.e.*, there is a significant amount of signal energy that is concentrated in just a few coefficients. Figs. 8 (a)-(b) show the corresponding HSI and CSI spectra when the object in Fig. 6 (a) is sampled with Hadamard and cosine basis. As a comparison, in Fig. 8 (c) shows the non-sparse spectrum associated to NSI in the same experiment. The patterns were ordered according to the zig-zag sorting procedure outlined in [38]. As can be seen in both Hadamard and cosine spectra, the largest amplitude coefficients are concentrated at the beginning of the signal and the remaining values are close to zero; whereas in the NSI spectrum the energy of the coefficients is distributed in the entire signal. These characteristics of HSI and CSI spectra allow reconstructing an object taking a fraction of the total data, attaining the same quality information of the reconstructed image [12, 25, 29, 38]. Fig. 9 shows PSNR values for different reconstruction ratios in HSI and CSI. When the reconstruction ratio exceeds ∼ 55%, the PSNR value is larger than 30 dB indicating high image fidelity.

In addition, Table 1 shows a quantitative comparison between
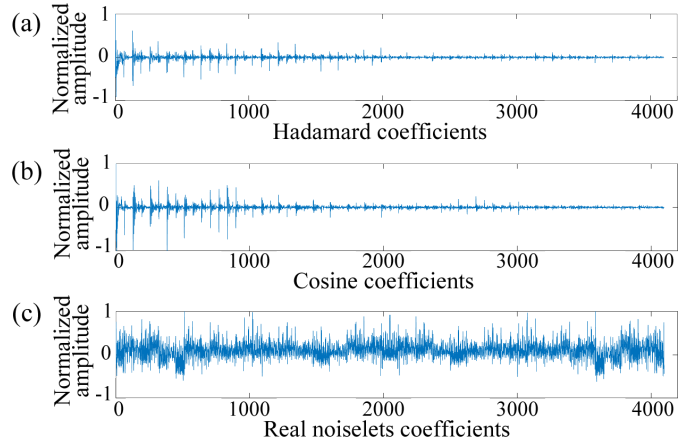
Fig. 8. Spectral coefficients of sampling basis (a) Hadamard, (b) cosine and (c) noiselet.

three different amplitude objects. The PSNR values were calculate as in the same conditions that the transparency UASLP-University logo. The amplitude objects are: a transparency with the Instituto de Investigación en Comunicación Óptica (IICO) logo, an insect wing, and a USAF resolution test chart. The results show that CSI can recover a high image fidelity. Note that the PSNR values for HSI and CSI are comparable.

As pointed out in Section 2.C, the proposed system can modu-

Table 1. Quantitative comparison of PSNR values for three amplitude objects. The size of each image is 64×64 pixels, and $880 \times 880 \ \mu m^2$.
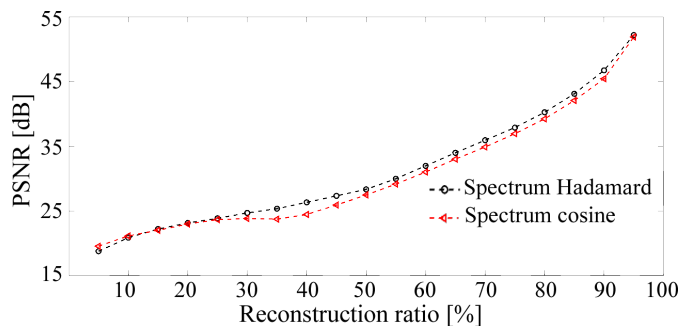
Object		PSNR values (dB)		
		HSI	CSI	NSI
IICO-logo		8.54	**8.87**	8.22
Wing		**16.06**	16.05	15.25
USAF		10.16	**10.58**	8.45

late phase, hence it is possible to compensate beam distortions created in the optical setup. For this, the wavefront phase distribution is measured in the absence of the object, and the result is introduced into Eq. (7) to be phase modulated through CGH.

The phase object analyzed is a semitransparent photoresist sample, which is used in photolithography processes. Figs. 10 (a)-(c) show the reconstructed phase distribution of the photoresist employing the sampling basis. For comparison, Fig. 10 (d) shows the phase measured by a CMOS camera by DH with the four-step phase-shifting, for which the camera resolution has been reduced to 64×64 pixels. The unwrapped phase map is calculated using the algorithm described in [48, 49], and the optical path length (OPL) is computed with

$$OPL = \frac{\Delta\varphi(x,y)\lambda}{2\pi},\tag{24}$$

where $\Delta\varphi(x,y)$ is the phase map and λ is the wavelength. Fig. 11 shows the one-dimensional OPL corresponding to the one-dimensional phase distribution obtained by Hadamard, cosine,

Fig. 9. PSNR values for different reconstruction ratios.
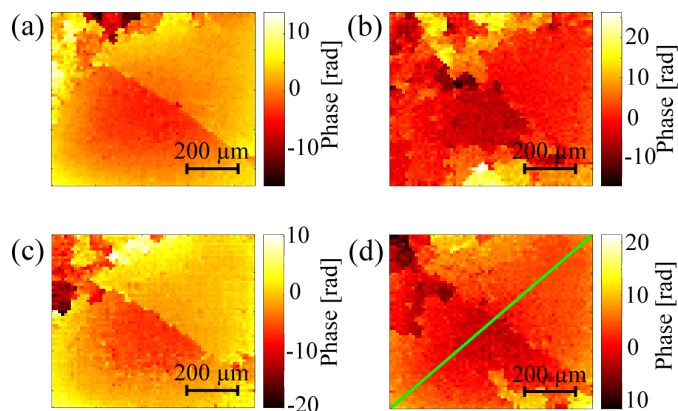
Fig. 10. Reconstruction of phase object with sampling basis (a) Hadamard, (b) cosine and (c) noiselet. (d) Reconstruction of the phase object with a CMOS camera.

and noiselet sampling, as well as with the CMOS camera. In Fig. 10 (d) the green line indicates the zone of interest of the OPL in Figs. 10 (a)-(c). The phase images demonstrate the sys-
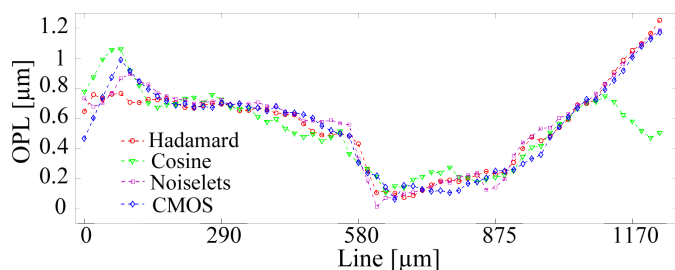
Fig. 11. Experimental results of single-pixel phase imaging. One dimensional phase distributions along the line in Fig. 10 (d).

tem ability to tackle complex information of an object, being the Hadamard and noiselet basis those that obtain a better reconstruction. As can be seen in Fig. 10 (b) the phase map measured with the cosine basis has a wrong phase in some regions, which could be due to loss of information using gray level codification (binarization) by dithering.

5. CONCLUSION

A DH microscopy system based on the SPI technique has been presented with a spatial resolution of 22 μm that retrieves both amplitude and phase images of complex objects. The experi-

mental results show a comparison between HSI, CSI, and NSI systems, validating the quality of results with PSNR values. The cosine basis recovered the one-dimensional amplitude distribution with best quality, with a PSNR value of 7.84 dB. An advantage of the presented approach is the high-speed binary modulation of the DMD to perform the registration process in less than four seconds for an object with 64×64 pixels. Furthermore, the differential measurement effectively restrains the noise generated by background lighting improving the quality of reconstructed images. Another advantage is that when using CGH, the modulation of the wavefront in both phase and amplitude imaging is possible, allowing to compensate the beam distortions in real-time. Finally, thanks to the sparsity property shown by Hadamard and cosine basis, we have shown that a good quality image can be reconstructed with only a fraction of the spectra, giving an opportunity to work in image compression methods or image systems based on CS. This work could provide guidance for choosing a SP imaging system aimed at different applications.

6. BACKMATTER

Disclosures. The authors declare no conflicts of interest.

REFERENCES

1. U. Schnars, C. Falldorf, J. Watson, and W. Jüptner, *Digital Holography and Wavefront Sensing* (Springer-Verlag Berlin, 2015).
2. U. Schnars and W. Jueptner, *Digital holography: Digital hologram recording, numerical reconstruction, and related techniques* (Springer Berlin Heidelberg, 2005).
3. M. K. Kim, *Digital Holographic Microscopy*, vol. 162 of *Springer Series in Optical Sciences* (Springer New York, New York, NY, 2011).
4. M. Kumar, O. Matoba, X. Quan, S. K. Rajput, Y. Awatsuji, and Y. Tamada, "Single-shot common-path off-axis digital holography: applications in bioimaging and optical metrology [Invited]," Appl. Opt. **60**, A195 (2021).
5. A. K. Singh, D. N. Naik, G. Pedrini, M. Takeda, and W. Osten, "Looking through a diffuser and around an opaque surface: A holographic approach," Opt. Express **22**, 7694 (2014).
6. F. Soldevila, V. Durán, P. Clemente, J. Lancis, and E. Tajahuerce, "Phase imaging by spatial wavefront sampling," Optica **5**, 164 (2018).
7. T. Tahara, K. Ito, T. Kakue, M. Fujii, Y. Shimozato, Y. Awatsuji, K. Nishio, S. Ura, T. Kubota, O. Matoba, J. W. Goodman, R. W. Lawrence, C. Poon, K. Doh, B. Schilling, M. Wu, K. Shinoda, Y. Suzuki, M. H. Jericho, H. J. Kreuzer, J. Sheng, E. Malkiel, J. Katz, J. Adolf, and R. Belas, "Parallel phase-shifting digital holographic microscopy," Biomed. Opt. Express **1**, 610 (2010).
8. O. Mendoza-Yero, E. Tajahuerce, J. Lancis, and J. Garcia-Sucerquia, "Diffractive digital lensless holographic microscopy with fine spectral tuning," Opt. Lett. **38**, 2107 (2013).
9. A. Anand, V. K. Chhaniwal, and B. Javidi, "Real-time digital holographic microscopy for phase contrast 3D imaging of dynamic phenomena," J. Disp. Technol. **6**, 500–505 (2010).

10. G. Singh and D. S. Mehta, "Measurement of change in refractive index in polymeric flexible substrates using wide field interferometry and digital fringe analysis," Appl. Opt. **51**, 8413 (2012).

11. S. Murata and N. Yasuda, "Potential of digital holography in particle measurement," Opt. Laser Technol. **32**, 567–574 (2000).

12. N. Radwell, K. J. Mitchell, G. M. Gibson, M. P. Edgar, R. Bowman, and M. J. Padgett, "Single-pixel infrared and visible microscope," Optica **1**, 285 (2014).

13. M. P. Edgar, G. M. Gibson, and M. J. Padgett, "Principles and prospects for single-pixel imaging," Nat. Photonics **13**, 13–20 (2019).

14. S. S. Welsh, M. P. Edgar, R. Bowman, P. Jonathan, B. Sun, and M. J. Padgett, "Fast full-color computational imaging with single-pixel detectors," Opt. Express **21**, 23068 (2013).

15. R. Horisaki, H. Matsui, R. Egami, and J. Tanida, "Single-pixel compressive diffractive imaging," Appl. Opt. **56**, 1353 (2017).

16. Z. Zhang, X. Wang, G. Zheng, and J. Zhong, "Fast Fourier single-pixel imaging via binary illumination," Sci. Reports **7**, 12029 (2017).

17. J. Huang, D. Shi, K. Yuan, S. Hu, and Y. Wang, "Computational-weighted Fourier single-pixel imaging via binary illumination," Opt. Express **26**, 16547 (2018).

18. E. Tajahuerce, V. Durán, P. Clemente, E. Irles, F. Soldevila, P. Andrés, and J. Lancis, "Image transmission through dynamic scattering media by single-pixel photodetection," Opt. Express **22**, 16945 (2014).

19. F. Soldevila, E. Salvador-Balaguer, P. Clemente, E. Tajahuerce, and J. Lancis, "High-resolution adaptive imaging with a single photodiode," Sci. Reports **5**, 14300 (2015).

20. X. Hu, H. Zhang, Q. Zhao, P. Yu, Y. Li, and L. Gong, "Single-pixel phase imaging by Fourier spectrum sampling," Appl. Phys. Lett. **114**, 051102 (2019).

21. Á. D. Rodríguez Jiménez, P. J. Clemente Pesudo, E. Tajahuerce, and J. Lancis, "Dual-mode optical microscope based on single-pixel imaging," Opt. Lasers Eng. **82**, 87–94 (2016).

22. P. Clemente, V. Durán, E. Tajahuerce, P. Andrés, V. Climent, and J. Lancis, "Compressive holography with a single-pixel detector," Opt. Lett. **38**, 2524 (2013).

23. L. Bian, J. Suo, Q. Dai, and F. Chen, "Experimental comparison of single-pixel imaging algorithms," J. Opt. Soc. Am. A **35**, 78 (2018).

24. M. Yao, Z. Cai, X. Qiu, S. Li, J. Peng, and J. Zhong, "Full-color light-field microscopy via single-pixel imaging," Opt. Express **28**, 6521 (2020).

25. Y. Chen, S. Liu, X. R. Yao, Q. Zhao, X. F. Liu, B. Liu, and G. J. Zhai, "Discrete cosine single-pixel microscopic compressive imaging via fast binary modulation," Opt. Commun. **454**, 124512 (2020).

26. H. Ren, S. Zhao, J. Gruska, D. V. Strekalov, A. V. Sergienko, D. N. Klyshko, Y. H. Shih, S. M. Zhao, H. Yang, Y. Q. Li, F. Cao, Y. B. Sheng, and W. W. Cheng, "Edge detection based on single-pixel imaging," Opt. Express **26**, 5501 (2018).

27. D. B. Conkey, A. M. Caravaca-Aguirre, E. Niv, and R. Piestun, "High-speed phase-control of wavefronts with binary amplitude DMD for light control through dynamic turbid media," Proc. SPIE **8617**, 86170I (2013).

28. L. Martínez-León, P. Clemente, Y. Mori, V. Climent, J. Lancis, and E. Tajahuerce, "Single-pixel digital holography with phase-encoded illumination," Opt. Express **25**, 4975 (2017).

29. B. L. Liu, Z. H. Yang, X. Liu, and L. A. Wu, "Coloured computational imaging with single-pixel detectors based on a 2D discrete cosine transform," J. Mod. Opt. **64**, 259–264 (2017).

30. J. H. Shapiro, "Computational ghost imaging," Phys. Rev. A **78**, 061802 (2008).

31. Y. Xiao, L. Zhou, and W. Chen, "Direct Single-Step Measurement of Hadamard Spectrum Using Single-Pixel Optical Detection," IEEE Photonics Technol. Lett. **31**, 845–848 (2019).

32. Y. Xiao, L. Zhou, and W. Chen, "Fourier Spectrum Retrieval in Single-Pixel Imaging," IEEE Photonics J. **11** (2019).

33. R. Horisaki, H. Matsui, and J. Tanida, "Single-pixel compressive diffractive imaging with structured illumination," Appl. Opt. **56**, 4085 (2017).

34. K. Komuro, Y. Yamazaki, and T. Nomura, "Transport-of-intensity computational ghost imaging," Appl. Opt. **57**, 4451 (2018).

35. S. Shin, K. Lee, Y. Baek, and Y. Park, "Reference-Free Single-Point Holographic Imaging and Realization of an Optical Bidirectional Transducer," Phys. Rev. Appl. **9**, 044042 (2018).

36. H. González, L. Martínez-León, F. Soldevila, M. Araiza-Esquivel, J. Lancis, and E. Tajahuerce, "High sampling rate single-pixel digital holography system employing a DMD and phase-encoded patterns," Opt. Express **26**, 20342 (2018).

37. Y. Endo, T. Tahara, and R. Okamoto, "Color single-pixel digital holography with a phase-encoded reference wave," Appl. Opt. **58**, G149–G154 (2019).

38. Z. Zhang, X. Wang, G. Zheng, and J. Zhong, "Hadamard single-pixel imaging versus Fourier single-pixel imaging," Opt. Express **25**, 19619 (2017).

39. S. S. Welsh, M. P. Edgar, R. Bowman, B. Sun, and M. J. Padgett, "Near video-rate linear Stokes imaging with single-pixel detectors," J. Opt. **17**, 025705 (2015).

40. S. L. Burnes-Rudecino, L. Martínez-León, P. J. Clemente Pesudo, E. Tajahuerce, and M. Araiza-Esquivel, "Alternative sampling functions for single-pixel imaging with a digital micromirror device," Proc. SPIE **10932**, 12 (2019).

41. S. Bouguezel, M. O. Ahmad, and M. N. Swamy, "Binary discrete cosine and hartley transforms," IEEE Transactions on Circuits Syst. I: Regul. Pap. **60**, 989–1002 (2013).

42. A. Pastuszczak, B. Szczygieł, M. Mikołajczyk, and R. Kotyński, "Efficient adaptation of complex-valued noiselet sensing matrices for compressed single-pixel imaging," Appl. Opt. **55**, 5141 (2016).

43. K. M. Czajkowski, A. Pastuszczak, and R. Kotyński, "Real-time single-pixel video imaging with Fourier domain regularization," Opt. Express **26**, 20009 (2018).

44. T. Tuma and P. Hurley, "On the incoherence of noiselet and Haar bases," in *SAMPTA'09,* (2009), p. General session.

45. E. Candès and J. Romberg, "Sparsity and incoherence in compressive sampling," Inverse Probl. **23**, 969 (2007).

46. W. H. Lee, "Binary computer-generated holograms," Appl. Opt. **18**, 3661 (1979).

47. R. A. Ulichney, "Dithering with Blue Noise," Proc. IEEE **76**, 56–79 (1988).

48. M. A. Herráez, D. R. Burton, M. J. Lalor, and M. A. Gdeisat, "Fast two-dimensional phase-unwrapping algorithm based on sorting by reliability following a noncontinuous path," Appl. Opt. **41**, 7437 (2002).

49. M. F. Kasim, "Fast 2D phase unwrapping implementation in MATLAB," https://github.com/mfkasim91/unwrap_phase/, (2017).